



# A filament modification approach for in situ ABS/OMMT nanocomposite development in extrusion-based 3D printing

Vishal Francis<sup>1</sup> · Prashant K. Jain<sup>1</sup>

Received: 8 October 2017 / Accepted: 27 June 2018 / Published online: 2 July 2018  
© The Brazilian Society of Mechanical Sciences and Engineering 2018

## Abstract

In the present study, a filament modification approach is proposed for in situ nanocomposite development during the 3D printing process. The acrylonitrile butadiene styrene filament was modified by coating it with organically modified montmorillonite (OMMT)-based nanocomposite solution. On 3D printing with the modified filament, a fused network of nanoparticles and polymer develops on the perimeter of the deposited raster's. This creates a unique mesostructure over the entire cross section of the 3D-printed part. Mechanical, thermal and dielectric properties were investigated to study the effect of filament alteration on 3D-printed parts. Microstructure and morphology of the nanocomposites were analyzed by XRD and SEM. The nanocomposite demonstrated 10.8% increment in Young's modulus compared to pristine polymer due to the presence of stiffer OMMT nanoparticles. The ionic nature of OMMT contributed in enhancing the relative permittivity of the nanocomposite by 64%. Thermal stability of the nanocomposite was also enhanced, and the glass transition temperature was increased by 6.7°C. Experimental data were compared with the rule of mixture and Halpin–Tsai composite models. Further, the mesostructure of 3D-printed parts was considered to modify the Halpin–Tsai composite model for 3D-printed parts.

**Keywords** Nanocomposite · Nanoclay · Organically modified montmorillonite · 3D printing · Fused deposition modeling

## 1 Introduction

Among various three-dimensional (3D) printing techniques, fused deposition modeling (FDM) has gained tremendous popularity over the years due to its inevitable advantages [1, 2]. Polymeric material in the form of the filament is utilized in FDM machine where they get heated in the liquefier and are deposited layer by layer as per the computer-aided design (CAD) model. The final part is fabricated as the layers are stacked with each other on solidification. The technique is widely used in biomedical, rapid tooling, aerospace, electromagnetics and prototyping

applications [3–7]. However, FDM parts lack behind in terms of material properties when compared with other polymer processing techniques like injection molding because of partial bonding between the layers and inherent porosity [8]. The use of nanofillers to enhance the material properties of polymers for FDM is gaining interest among industries and researchers. Nanofillers such as carbon nanotube [9, 10], organically modified montmorillonite (layered silicate/nanoclay) [11, 12], nanographene platelets [13] and carbon nanofiber [14], which have high aspect ratios, can provide significant improvements even at very low filler loadings [1, 15, 16]. However, the stage at which the nanoparticle is added also plays an important role in altering the material properties of the 3D-printed part. Most of the studies conducted for the inclusion of nanofiller demonstrate nanocomposite formation in a pre-processing stage prior to the printing process. This requires an extra processing step and equipment. However, in FDM process, in situ nanocomposite formation can also be achieved. There is a scarcity of information regarding the in situ development of nanocomposites. This creates a need to

---

Technical Editor: Márcio Bacci da Silva.

✉ Vishal Francis  
f.vishal@iiitdmj.ac.in  
Prashant K. Jain  
pkjain@iiitdmj.ac.in

<sup>1</sup> Mechanical Engineering Discipline, PDPM Indian Institute of Information Technology, Design and Manufacturing Jabalpur, Jabalpur, Madhya Pradesh 482005, India

investigate the effect of in situ nanocomposite development on the material properties of FDM parts.

Among the various nanoparticles used for developing polymer nanocomposite, OMMT is one of the most investigated candidates. OMMT nanoparticles are easily available, economically attractive and demonstrates excellent enhancement in various material properties such as tensile strength, Young's modulus, permeability, thermal stability, dielectric, hardness, heat deflection temperature, flame retardancy and dimensional stability [11, 12, 16–20]. The literature reveals that organically modified montmorillonite (OMMT) has been previously utilized in 3D printing techniques. Yen et al. [18] prepared OMMT-based nanocomposite via solution method and reported significant improvement in tensile strength, Young's modulus, flexural and impact strength. Evidence of nanocomposite formation was also reported for nylon 12/clay nanocomposite [11]. Polyamide/clay nanocomposite exhibited increased tensile strength and Young's modulus along with improved flexural strength [12]. However, the stiff nanoparticles tend to decrease the elongation at break. OMMT has been mainly used for powder-based technique and its potential is not fully explored for extrusion-based 3D printing technique.

In order to explore the effect of OMMT on FDM 3D-printed parts, a unique approach has been utilized by coating the acrylonitrile butadiene styrene (ABS) filament with ABS/OMMT solution. This approach provides an effective way to develop in situ nanocomposite during FDM process. Moreover, it helps to reduce the time span for 3D printing of nanocomposites by eliminating the filament fabrication step required when melt mixing the nanoparticles. Moreover, this coating approach is potentially capable of improving the material properties of the polymer [10–14]. In addition, the benefit of coating OMMT nanoparticles on polymer filament compared to mixing is that the surface area of dispersed nanoparticles can be reduced. This situation is favorable for enhancement of dielectric properties of OMMT-based nanocomposites. Since highly dispersed OMMT nanoparticles can suppress the dipole polarization of ABS polymer chains [19, 20], the proposed approach can be utilized to 3D print dielectric substrates for wireless communication devices such as microstrip patch antenna and Fresnel lens. The compatibility of ABS with OMMT has been already reported for techniques other than 3D printing, and enhancement in mechanical and thermal properties was observed [21–24]. In the present work, ABS/OMMT solutions were prepared to modify the ABS filament for FDM process. Mechanical, thermal and dielectric properties were evaluated and compared with the pristine polymer. Figure 1 shows the filament modification approach and the testing process for the nanocomposite.

## 2 Materials and methods

### 2.1 Materials

Organically modified montmorillonite (Cloisite 30B) was purchased from Nanoshel-Intelligent Material Pvt. Ltd. The organic modifier used in Cloisite 30B is MT2EtOH (methyl, tallow, bis-2-hydroxyethyl, quaternary ammonium). Layered silicates are hydrophilic in nature, and organic modification is essential to provide compatibility with hydrophobic polymers [25]. The modifier concentration is 90 meq/100 g clay. ABS (acrylonitrile butadiene styrene) filament was supplied by the machine manufacturer (FDM 3D printer Flashforge creator pro).

### 2.2 Filament modification for 3D printing

First, 20 grams of ABS was solubilized in 100 ml of dimethyl ketone and consecutively the required amount of OMMT powder was swelled in the solution by mixing it for an hour using a magnetic stirrer [26] at room temperature (Fig. 1). The process was carried out with 0.2, 0.6 and 1 g of OMMT to get three different proportions of OMMT (1, 3 and 5 wt%) in ABS matrix. The prepared solutions were dip-coated over the ABS filament. The filament diameter before coating was 1.75 mm (commercially available size), and after coating the achieved diameter was  $1.85 \pm 0.04$  mm. The coating time was adjusted in preliminary experiments in order to maintain the diameter of the filament under 1.9 mm due to the machine constraint. The volume percentage of the coated layer on the ABS filament was 10.5%. Therefore, after coating the percentage of nanoclay in filaments was 0.1, 0.3 and 0.5 wt%, respectively. Further, the modified filament was exposed to microwave irradiation for 1 min. The hydroxyl group present in the organic modifier of Cloisite 30B responds on microwave irradiation and rotates causing heat and shear environment which can overcome Van der Waals force between the clay layers and helps in exfoliation of clay. A domestic microwave was used with 800 W maximum power. On observing the surface of the modified filament (Fig. 5), the presence of nanoparticles was evident. It was found that nanoparticles were dispersed across the surface of the specimens due to the homogeneity of the coating over the polymer filament. After the removal of the solvent, the filament was fed into the FDM 3D printer for specimen fabrication. NC 1, NC 3 and NC 5 correspond to filaments containing 0.1, 0.3 and 0.5 wt% OMMT. Figure 2 shows the schematic diagram of 3D-printed part with modified filament demonstrating the fused network of polymer and layered silicate (OMMT) developed during 3D printing. The red arrows illustrate the presence of OMMT.

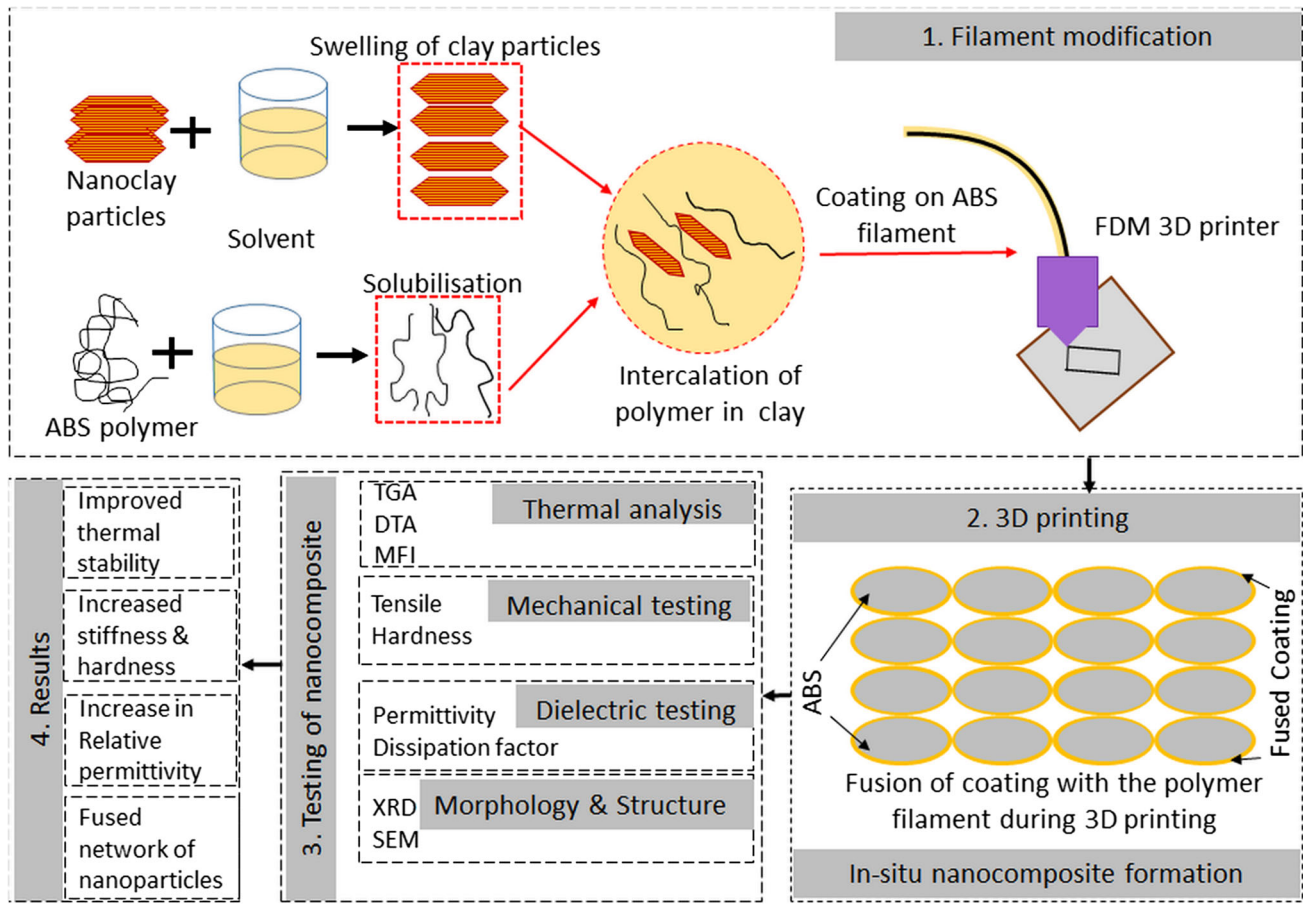


Fig. 1 Flowchart showing filament modification and testing process for the nanocomposite

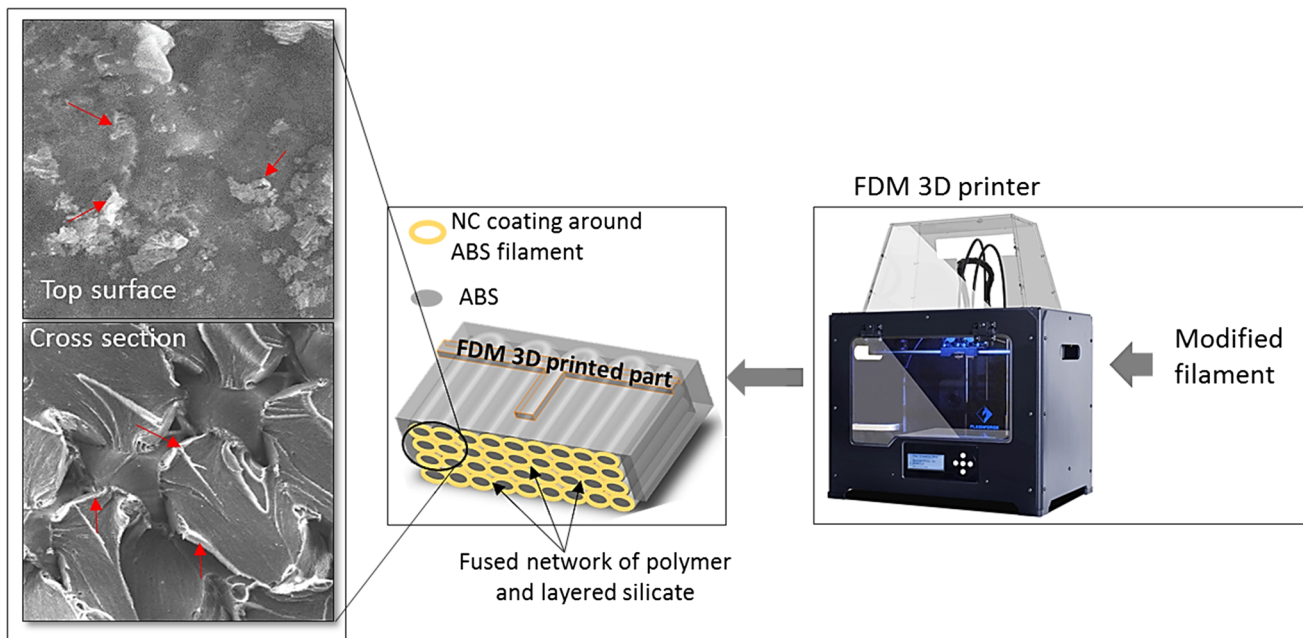


Fig. 2 Schematic representation of a fused network of polymer and OMMT developed during 3D printing

## 2.3 Specimen preparation

A dual extruder FDM 3D printer (Creator Pro, Zhejiang Flashforge 3D Technology Co., Ltd) was used to print the specimens with pristine and modified ABS filament. For mechanical studies of 3D-printed specimens, tensile specimens were fabricated with dimensions similar to ASTM D 638-10 and three replicates were tested. For hardness testing, specimens were designed according to ASTM D2240-03 (Shore D) and three readings were recorded on the top surface of the specimens parallel to the laid rasters. For permittivity extraction (dielectric testing), the substrates were printed with dimensions of  $25 \times 18 \times 1.5$  mm. A copper transmission line (width 1.8 mm) with quarter wavelength open stub (for 8 GHz) was adhered on the printed substrates using epoxy glue for extraction of dielectric properties. Three replicates were tested for permittivity extraction. The frequency range for testing was from 2 GHz to 10 GHz. The details of the 3D-printed specimens for all the testings are shown in Table 1.

Preliminary experiments were conducted to adjust the extruder temperature for the coated filament, and it was found that the nanocomposite-coated filaments require higher extruder temperature compared to ABS filament during 3D printing. Therefore, the extruder temperature was increased and kept at  $245^\circ\text{C}$  for the nanocomposites and  $230^\circ\text{C}$  for ABS specimens. The bed temperature was maintained at  $110^\circ\text{C}$  for all the specimens. 100% infill was used for printing the specimens. Raster angle was kept at  $0^\circ$ . Raft support was used at the bottom of the specimens to




ensure no warping occurs during printing. During 3D printing, the coating fuses with the core filament as it is heated inside the heater. Further, as the deposited raster fuses with the neighboring raster, the coating also fuses with the neighboring raster; this creates an interconnected fused network of coating and polymer over the entire cross section of the part. The 3D printing parameters selected for fabrication of specimens are illustrated in Fig. 3.

## 2.4 Characterization

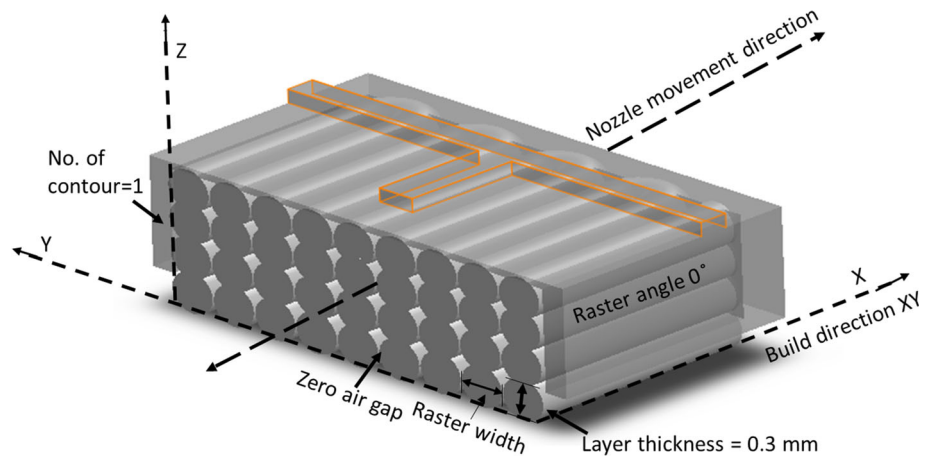
### 2.4.1 X-ray diffraction and scanning electron microscopy

The microstructure of the nanocomposites was investigated by XRD technique. An X-ray diffractometer (AXS D8 advance Bruker) was used with specifications as, X-ray source-Cu, wavelength  $1.5406 \text{ \AA}$ , generator working at 40 kV and 35 mA, maximum usable angular range  $3^\circ$ – $135^\circ$  and a step size of  $0.020^\circ$ . The d-spacing of clay layers was obtained from Bragg's rule. For XRD analysis, the samples were cut from the 3D-printed specimens. The tests were performed at room temperature. The morphology of the nanocomposite was observed by SEM (JEOL model JSM-690LV), magnification  $5\times$ – $300,000\times$  and accelerating voltage of 20 kV. For SEM analysis, the samples were taken from the top surface and cross section (fractured part) of 3D-printed tensile specimens.

**Table 1** Details of 3D-printed specimens fabricated for mechanical and dielectric testing

Type of specimen	Test conditions	No. of specimens	Geometry	Dimensions (mm)
Tensile	Crosshead speed: 10 mm/min, room temperature	ABS-03		Length 63.5
		NC 1-03		Thickness 3.2
		NC 3-03		Width 9.53
		NC 5-03		Gauge length 9.53
Hardness	Shore: D, room temperature	ABS-03		Gauge width 3.18
		NC 1-03		Length 50
		NC 3-03		Thickness 6.5
		NC 5-03		Width 50
Dielectric (quarter wavelength open stub resonator)	Frequency: 2–10 GHz, room temperature	ABS-03		Length 25
		NC 1-03		Thickness 1.5
		NC 3-03		Width 18
		NC 5-03		Open stub width 1.8

**Fig. 3** 3D printing parameters for fabrication of test specimens



**2.4.2 Thermal analysis**

Thermal analysis was carried out utilizing TG/DTA instrument (PerkinElmer) with temperature range from ambient to 1200 °C. Twenty grams of samples was heated from 40 °C to 740 °C at a rate of 20 °C/min in the nitrogen atmosphere. The samples were taken from the printed specimens. The microscope images were taken by digital microscope (Celestron). Melt flow indexer (Oracle equipments) was used to observe the melt flow behavior of the nanocomposite according to ASTM D 1238-95.

**2.4.3 Mechanical and dielectric testing**

The tensile testing was performed on a Tinius Olsen testing machine with a crosshead speed of 10 mm/min. Hardness test was conducted on a durometer (Yuzuki). A vector network analyzer (Agilent E5071C) was used to get plot between frequency and scattering parameter for extraction of dielectric values. All the mechanical and dielectric testings were performed at room temperature.

**2.5 Permittivity extraction**

The relative permittivity was extracted using quarter wavelength open stub resonator, the process as demonstrated by a flowchart in Fig. 4 [27] where L is the length of the open stub, n is the resonance number, and w and h are the width of copper transmission line and thickness of the substrate, respectively. S<sub>21</sub> data are obtained from the network analyzer. Effective permittivity is calculated as:

$$\epsilon_{\text{eff}} = \left( \frac{(2n - 1)c}{4f_0(l + \Delta l)} \right)^2 \tag{1}$$

where f<sub>0</sub> is the resonating frequency and can be calculated as Eq. 2

$$f_0 = (f_l + f_h)/2 \tag{2}$$

In Eq. 2, f<sub>l</sub> and f<sub>h</sub> correspond to lower and upper frequencies of the 3-dB insertion loss. The length of the stub is denoted by l, Δl is the adjusted length calculated according to Kirschning et al. [28], c is the speed of light in free space, and n is the resonance number, n = 1 that corresponds to the central resonance frequency

Relative permittivity can be calculated from the following expression:

$$\epsilon_{\text{eff}} = \frac{\epsilon_r + 1}{2} + \frac{\epsilon_r - 1}{2} \left( 1 + 12 \left( \frac{h}{w} \right) \right)^{-0.5} \tag{3}$$

The Kirschning approach can be found in the literature [28]. When the deviation in relative permittivity, effective permittivity and Δl is insignificant, the procedure is stopped.

**2.6 Composite model for prediction of Young’s modulus**

The prediction of Young’s modulus was carried out using Halpin–Tsai composite model and rule of mixture. Further, the mesostructure of 3D printed parts was considered to calculate their void volume. The modifications were incorporated in the Halpin–Tsai model and compared with the experimental results (discussed in Sect. 3.5).

Halpin–Tsai composite model [37] for prediction of Young’s modulus is given as follows:

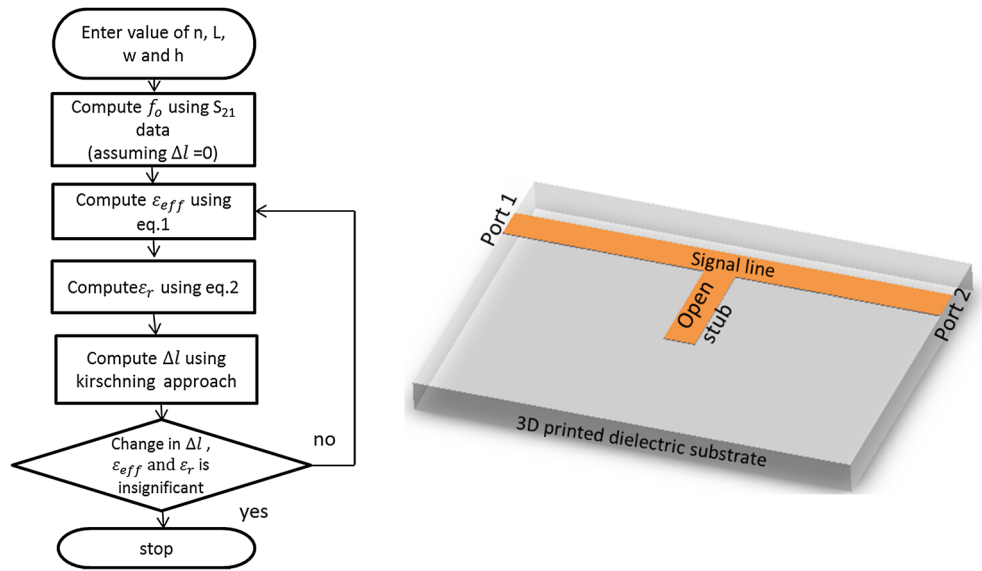
$$\frac{E_c}{E_m} = \frac{(1 + \zeta \eta \phi)}{(1 - \eta \phi)} \tag{4}$$

where E<sub>c</sub>, E<sub>f</sub> and E<sub>m</sub> are the composite, filler and matrix Young’s modulus in Pascal. ζ is the shape parameter, and for clay platelets it is taken as {2/3\* (L/T)} [38], where L and T are the length and thickness of clay platelets in nm. η is given by Eq. 5.

$$\eta = [(E_f/E_m) - 1]/[(E_f/E_m) + \zeta] \tag{5}$$

And φ is the volume fraction of filler and is calculated as:

**Fig. 4** Flowchart and schematic diagram of specimen used for permittivity extraction



$$\phi = \frac{(w_f/\rho_f)}{[(W_f/\rho_f) + (1 - W_f)/\rho_m]} \tag{6}$$

where  $W_f$ ,  $\rho_f$  and  $\rho_m$  are the weight of filler in (g), and density of fiber and matrix in ( $g/cm^3$ ).

Young’s modulus according to rule of mixture (RoM) is calculated as follows.

$$\text{Young’s Modulus } E_1 = E_f V_f + E_m V_m \tag{7}$$

where  $E_f$  and  $E_m$  are the fiber and matrix Young’s modulus in Pascal, and  $V_f$  and  $V_m$  are the volume fraction of fiber and matric, respectively. The parameters considered for the prediction using composite models are shown in Table 2.

### 3 Results and discussion

#### 3.1 Microstructure and morphology of 3D-printed nanocomposite

The microstructure and morphology of the nanocomposites were observed by XRD and SEM techniques. The composite microstructures are shown in Fig. 5. OMMT shows a diffraction peak at  $4.75^\circ$  (2 theta value) which corresponds to d-spacing of 1.85 nm (nm) due to its regular layered structure [29]. Due to the ABS matrix, the nanocomposites

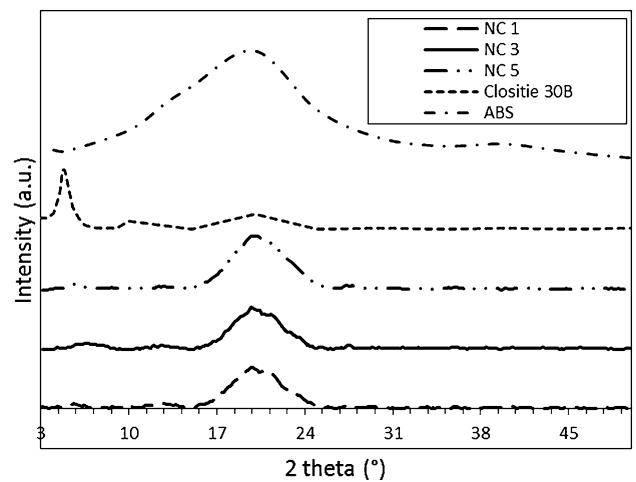


**Fig. 5** X-ray spectra of ABS, OMMT and nanocomposites

showed broad peaks around  $20^\circ$  because of its amorphous structure. On observing the diffraction pattern of nanocomposites near OMMT diffraction peak, no peaks were identified and all the three compositions followed almost the same diffraction pattern. The absence of peak suggests good dispersion of OMMT in the ABS matrix [30] and seems to be a plausible reason for exfoliation and absence of large tactoids [29]. However, Small shoulders were also observed around  $2\theta = 5.5$  for NC 1 and NC 3 and

**Table 2** Parameters considered for composite modeling

Composite model	Parameters used for calculations
Halpin–Tsai and rule of mixture	$\zeta = 2/3 * L/T$ ( $L = 100$ & $D = 1$ ) [38, 40], $\rho_f = 1.98$ [41], $\rho_m = 1.05$ [14], $E_f = 170 \times 10^9$ [41], $E_m(\text{abs}) = 1199 \times 10^6$ , $E_m(\text{NC1}) = 1263 \times 10^6$ , $E_m(\text{NC3}) = 1314 \times 10^6$ , $E_m(\text{NC5}) = 1328 \times 10^6$ , $w_{f1} = 0.00465$ , $w_{f2} = 0.00480$ , $w_{f3} = 0.00482$ ,

$2\theta = 6.0^\circ$  for NC 5 nanocomposites which may be due to the agglomeration of some clay layers [31]. Therefore, the nanocomposite structure may have exfoliated clay platelets along with some clay tactoids.

SEM analysis of the top surface of 3D-printed parts revealed the presence of OMMT particles on each printed raster. Figure 6 demonstrates the SEM images at various magnifications for NC 3 and NC 5 nanocomposites. The bright surfaces in the image are the clay particles, whereas darker region is the ABS matrix. OMMT particles were distributed over the entire observed specimens suggesting good dispersion which was also evident from the XRD analysis. However, certain clay tactoids of few microns were also observed. The OMMT coating fuses with the

ABS core filament and the neighboring filaments during 3D printing creating a fused network of polymer and layered silicate at the raster–raster interface and at the outer surfaces of the printed part. Figure 6g–i demonstrates rasters and the bonding between the raster's (neck formations) in the 3D-printed parts. The dashed circle shows the voids present inside the 3D-printed part. Due to rapid cooling of the deposited raster's, partial bonding is achieved between them. This creates an inherent porosity within the cross section of the 3D-printed specimens as voids even if 100% infill is selected for printing [32].

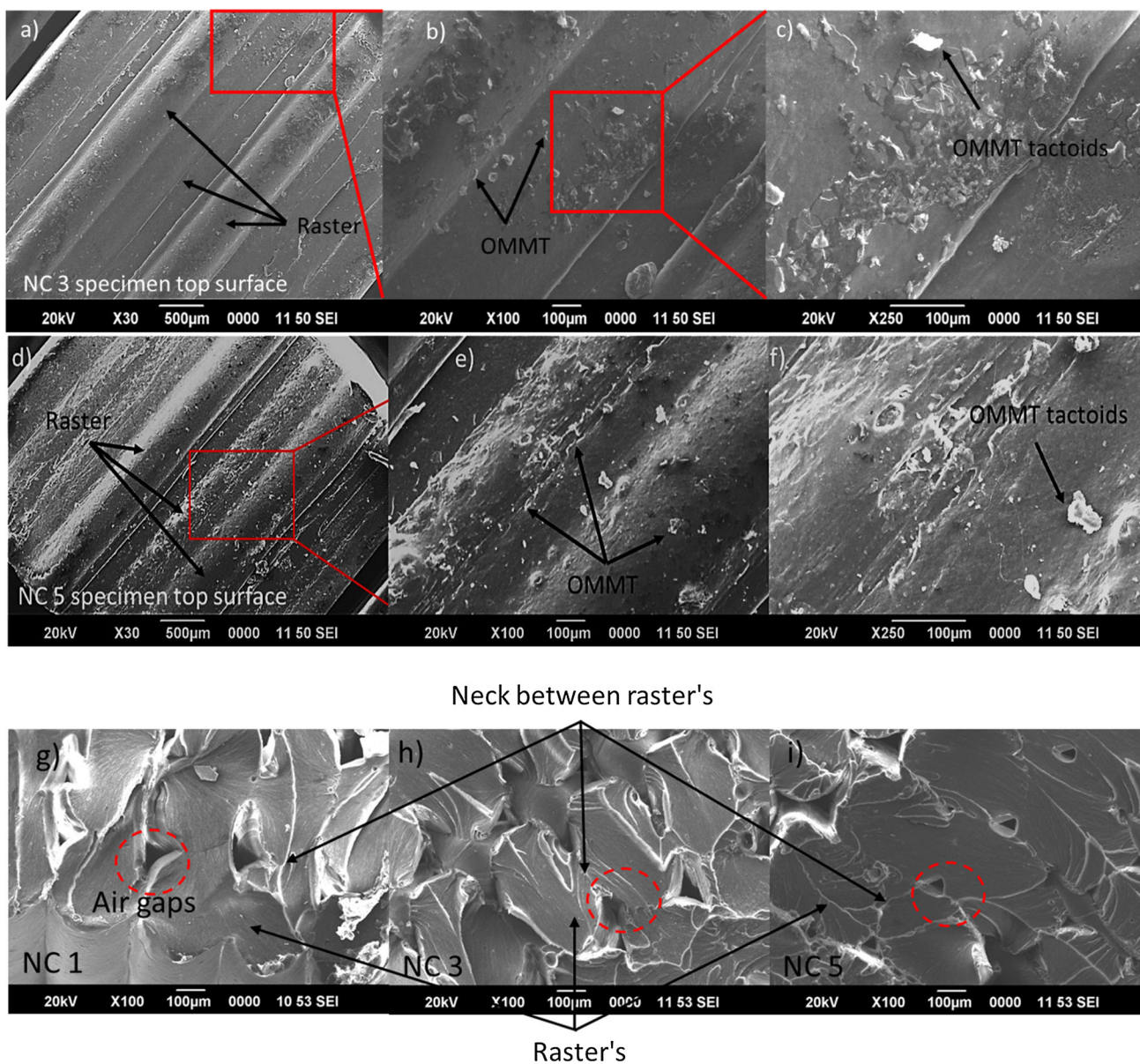


Fig. 6 SEM images of 3D-printed nanocomposites (a–f) top surface and (g–i) cross section

### 3.2 Mechanical properties

The typical stress–strain curves for each 3D-printed specimen fabricated with ABS and nanocomposites are shown in Fig. 7. The ultimate tensile stress of the nanocomposites did not show a significant improvement compared to pristine ABS polymer, a marginal increase was observed for NC 1 and NC 3 nanocomposites. However, a slight decrease was observed for NC 5 nanocomposite (Fig. 7 inset). This may be due to the larger clay tactoids present in NC 5 which might have acted as defects.

Figure 8 shows the effect of OMMT on Young's modulus and elongation at break for the composites. The incorporation of OMMT increased Young's modulus of the nanocomposites. OMMT being stiffer partner provided reinforcement at the polymer/clay interface. Since these nanoparticles have higher modulus and strength compared to pristine ABS, their well-dispersed presence in the polymer matrix increased Young's modulus of the 3D-printed parts. NC 5 showed 10.8% increment, whereas NC 3 and NC 1 showed 9.6 and 5.3% increment, respectively, from pristine ABS (Fig. 8). It can be also seen in the figure (secondary axis) that as the nanofiller loading increases from NC 1 to NC 5, the elongation at break decreases. This decrease is due to the restriction offered by OMMT nanoparticles in the mobility of ABS molecular chains, which makes the nanocomposite stiffer than pristine ABS. Similar behavior of OMMT-based polymer composites was observed in the previous literature [22].

Moreover, by observing the fractured surfaces of the nanocomposites, the change in elongation at break can be understood. Figure 9 shows the fractured surface of 3D-printed nanocomposites. NC 1, which exhibits a greater elongation at break compared to NC 3 and NC 5, shows more plastic deformation as demonstrated by fibril structure (Fig. 9a). As the OMMT loading has increased the elongation at break decreased, yielding a much smoother fractured surface as shown in Fig. 9b, c. Since OMMT is

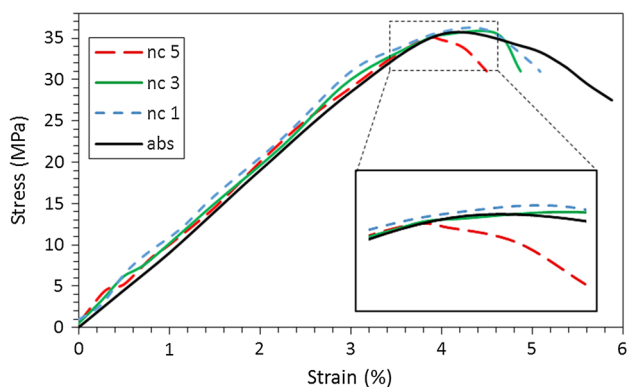


Fig. 7 Stress versus strain graph for ABS and nanocomposites

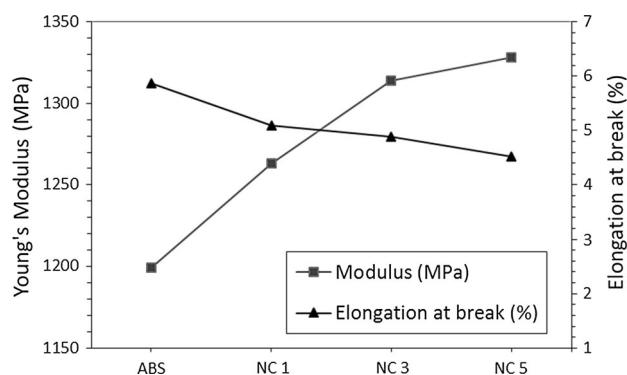


Fig. 8 Young's modulus and elongation at break of 3D-printed ABS and nanocomposites

much stiffer than ABS polymer, their presence contributes to brittle fracture in the nanocomposites and thereby decreases the elongation at break as filler loading was increased.

Figure 10 shows the change in hardness values for the nanocomposites compared to pristine ABS. Due to ABS/OMMT coating on the filament, the 3D-printed parts have a network of OMMT along the cross section and also on the surface, and since they are rigid in nature, they contributed in altering the hardness of printed parts. The ceramic nature of OMMT offered resistance to indentation; therefore, NC 3 and NC 5 showed 5.25 and 4.56% increment, whereas NC 1 showed a very marginal increment of 2.5% from the base polymer material.

### 3.3 Thermal properties and melt flow index

Thermal analysis was performed to observe the effect of OMMT coating on the thermal stability of 3D-printed ABS nanocomposites. Thermogravimetric analysis (TGA) and differential thermal analysis (DTA) were used for this purpose. Figure 11 demonstrates a TGA curve for the nanocomposites and pristine ABS. It can be seen from the figure that 90% of the mass loss occurred around 370 °C for pristine ABS and around 390 °C for the nanocomposites. The materials demonstrated two-stage decomposition process. In the first stage, the mass loss peak appeared around 430 °C (inflection point) and in the second stage, the peak was observed around 560–590 °C (Fig. 12). The decomposition of the nanocomposites was toward higher temperature compared to pristine ABS. OMMT works as thermal insulators, thereby increasing the thermal stability of the polymer.

Figure 13 shows the DTA curve for the nanocomposites. The glass transition temperature ( $T_g$ ) of the nanocomposites showed an increasing trend as the OMMT weight percent was increased. For NC 5, the value of  $T_g$  was 105 °C, which is around 6 °C greater than the  $T_g$  of pristine



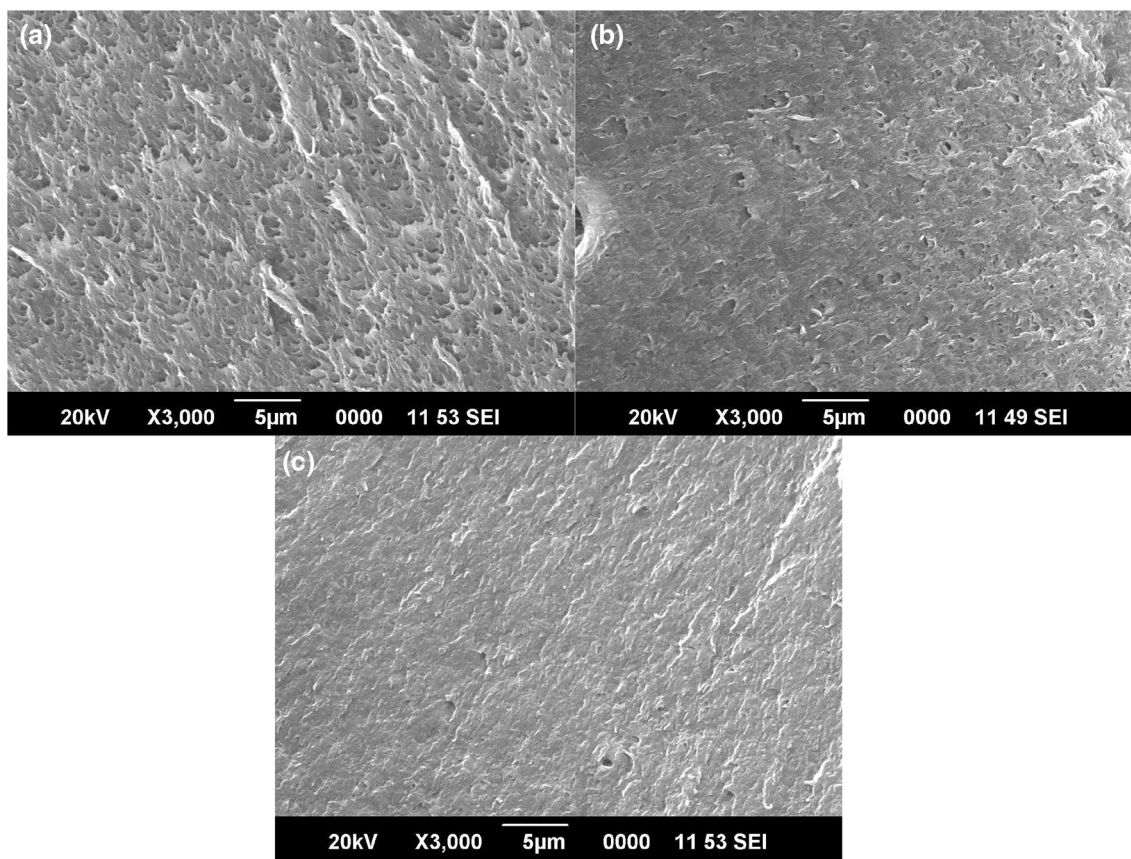


Fig. 9 Fractured surfaces of nanocomposites a NC 1, b NC 3 and c NC 5

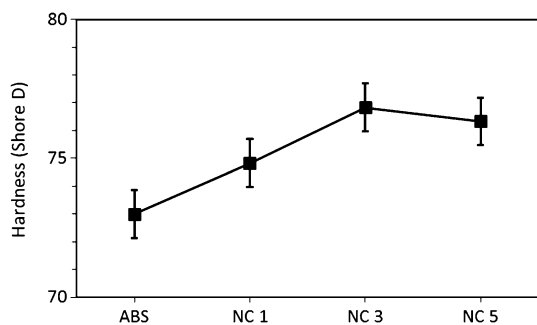


Fig. 10 Comparison of hardness between 3D-printed ABS and nanocomposites

ABS used. For NC 1 and NC 3, the value of  $T_g$  was 100 °C and 102 °C, respectively. The restriction in the segmental motion of the molecules provided by OMMT interaction with the polymeric chains provided an increment in the glass transition temperature of the nanocomposites.

The melt flow index (MFI) of the nanocomposite and pristine ABS was investigated at 220 °C, and their values are listed in Table 3. It is clear from the tabulated values that the high aspect ratio OMMT has decreased the MFI value of ABS, thereby increasing the viscosity of the nanocomposite. Interaction of clay layers with ABS offered

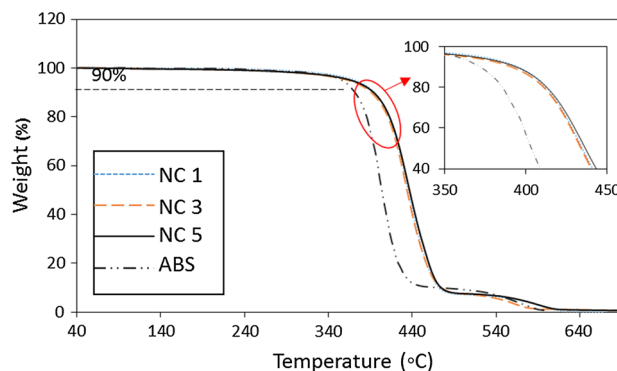
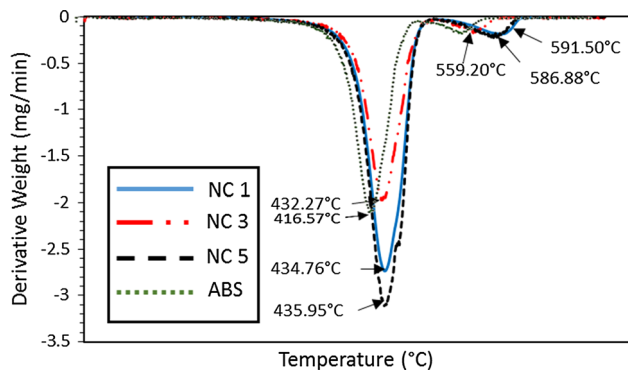


Fig. 11 TGA curve demonstrating weight loss (%) of ABS and nanocomposites with respect to increasing temperature

restriction in the melt flow of the nanocomposites as it was also observed by the increase in  $T_g$ ; therefore, 3D printing of ABS/OMMT nanocomposite required higher extruder temperature than pristine ABS.

### 3.4 Dielectric properties

The dielectric properties such as relative permittivity and loss tangent were extracted using a quarter wavelength open stub resonator. Figure 14 shows the graph between



**Fig. 12** Derivative of weight change versus temperature of ABS and nanocomposites showing inflection point and their decomposition

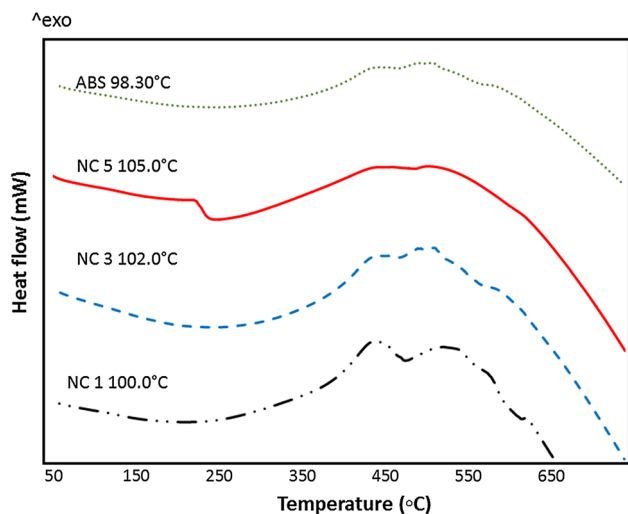


**Fig. 13** DTA curve for the nanocomposites

**Table 3** MFI values for the pristine ABS and nanocomposites

S. no.	Material	MFI g/10 min (220 °C and 2.105 kg load)	SD
1	ABS	1.5	0.075
2	NC 1	0.84	0.085
3	NC 3	0.72	0.028
4	NC 5	0.60	0.049

scattering parameter S21 and frequency for ABS and nanocomposites. The resonating frequencies of nanocomposite substrates were found to be at lower frequencies compared to pristine ABS substrate. The relative permittivity of ABS substrates was found to be 2.42; the data are in good agreement with the previous work reported [32, 33]. However, the value increased for the nanocomposites along with the increase in loss tangent compared to pristine ABS. An increment of 1.49, 1.50 and 1.55 was

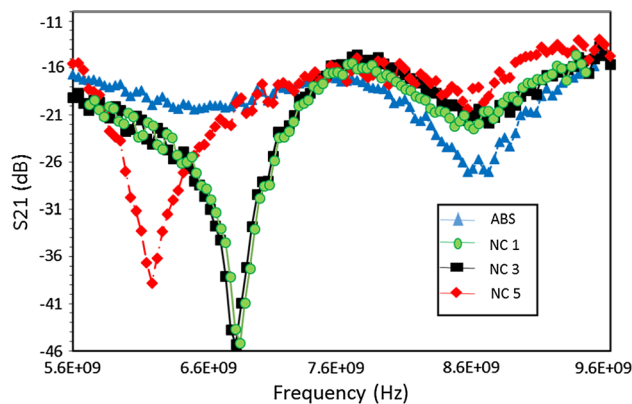


**Fig. 14** Measured S21 parameter vs frequency plot for the quarter wavelength open stub resonator

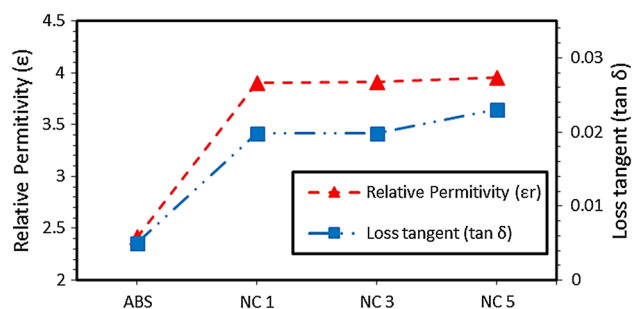


**Fig. 15** Relative permittivity and loss tangent of ABS and nanocomposites

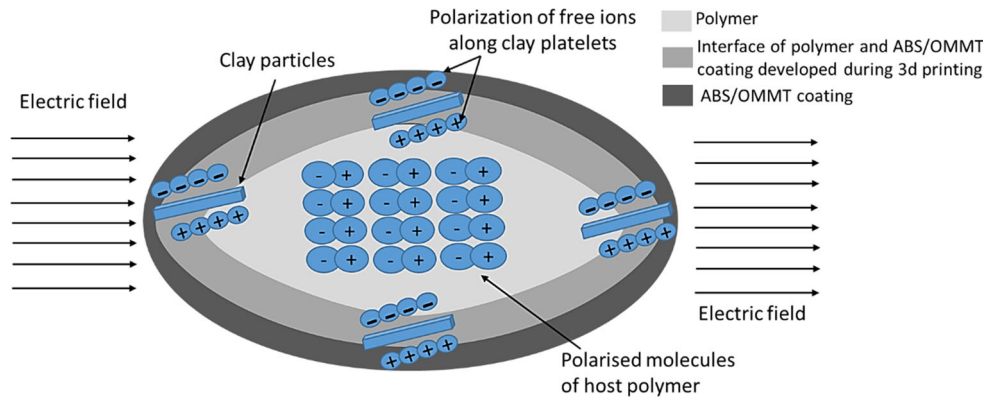
observed in NC 1, NC 3 and NC 5 permittivity values, respectively (Fig. 15).

Loss tangent value for ABS was 0.005, and that for NC 1, NC 3 and NC 5 was 0.019, 0.019 and 0.023, respectively. OMMT is ionic in nature and provided additional polarization mechanisms to the overall polarization of ABS material. An interfacial polarization is developed at the interface of OMMT and ABS. Further, the free ions present in OMMT contributed to ionic polarization, thereby increasing the permittivity of nanocomposites (Fig. 16). The increment in dielectric values for clay-based composite systems has also been reported previously [19, 20, 34–36].

### 3.5 Young’s modulus prediction

The predicted values by Halpin–Tsai model and rule of mixture are shown in Fig. 17. It is clear from the graph that rule of mixture is not very suitable for the prediction of Young’s modulus since it does not consider the interaction of the constituent of the composite. However, Halpin–Tsai model prediction was in good agreement for low OMMT loading. As the loading was increased, the difference between the predicted and the experimental values increased. The difference in Halpin–Tsai model and

**Fig. 16** Schematic showing the additional polarization mechanism due to filament modification with OMMT



experimental values may be due to the following reasons. Firstly as the filler loading increases, the tendency of agglomeration of OMMT layers also increases, which tends to reduce the load-bearing capacity of the filler. And secondly, due to the inherent voids present in the mesostructure of the FDM parts. These voids reduce the effective volume fraction considered for prediction. Therefore, the predicted results will deviate from the experimental values.

Therefore, in order to accommodate this change, the mesostructure of the FDM parts was observed under a microscope to measure the filament height and width (Fig. 18). Halpin–Tsai model was modified based on the mesostructure.

Table 4 shows the average measured filament height and width values for ABS and the nanocomposites. Since the size of the voids may vary from bottom to top of the part (bottom layers contains smaller voids compared to top layers [39]), the measurement was taken from the bottom, middle and top deposited layers. Three readings were taken from each layer, and then, the average values were considered for calculations.

Figure 19 shows the graphical illustration of mesostructure of FDM printed parts, where the elliptical shapes represent the laid filament and dark area represents

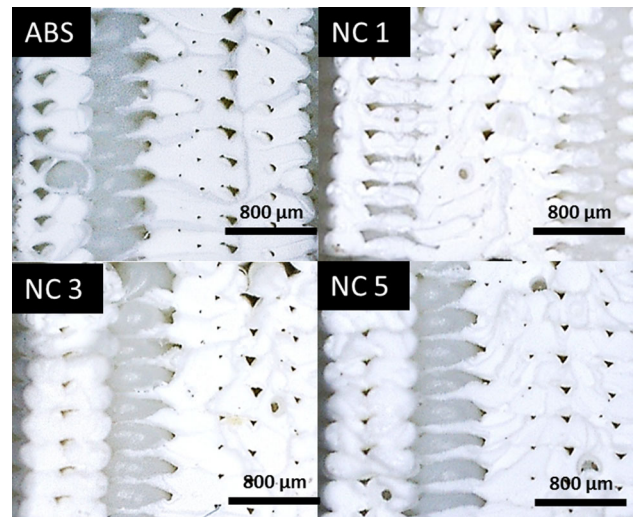


**Fig. 18** Mesostructure of 3D-sprinted parts (pristine ABS and nanocomposites)

the voids. The desired geometry is approximated by these bonded laid filaments. The elliptical shape of the filaments can be used to derive a relation between ellipse axes and void volume as shown in Eq. 8.

$$v = \left[ \frac{t}{2b} \cdot \frac{w}{2a} (2a \cdot 2b - \pi ab) \right] l \tag{8}$$

where  $t$  and  $w$  are the thickness and width in mm of the specimen,  $2a$  and  $2b$  are the major and the minor axis of elliptical filament, respectively, and  $l$  is the gauge length.

**Table 4** Measured width and height of deposited filament in mesostructure of FDM part

S. no.	Material	Height <sub>Avg</sub> (mm)	Width <sub>Avg</sub> (mm)
1	ABS	0.29	0.39
2	NC 1	0.30	0.42
3	NC 3	0.30	0.41
4	NC 5	0.30	0.40

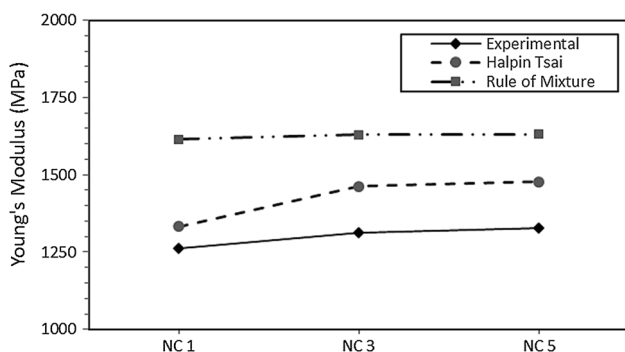


**Fig. 17** Comparison of experimental and predicted values for Young's modulus by Halpin–Tsai and rule of mixture

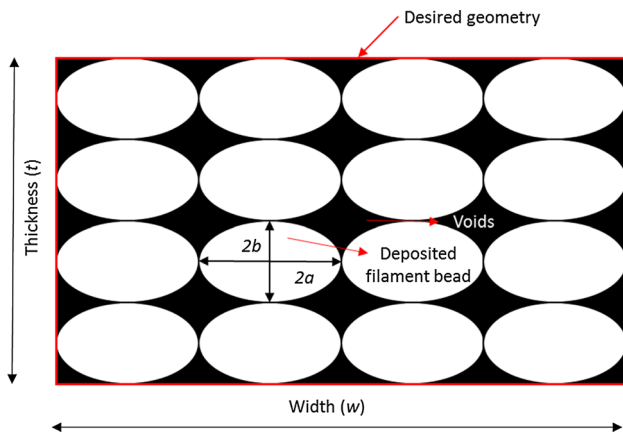


**Fig. 19** Graphical illustration of 3D-printed mesostructure showing voids formed between the deposited filaments

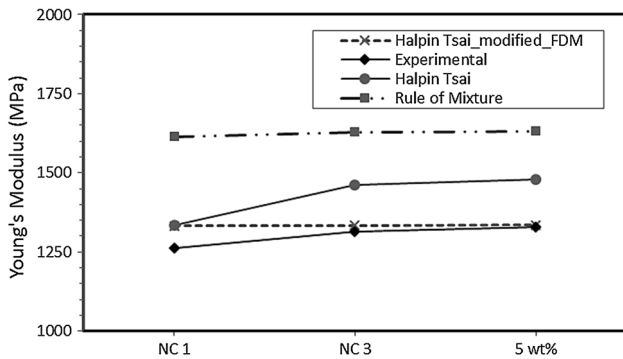


**Fig. 20** Comparison of experimental and predicted values of Young's modulus by modified Halpin–Tsai, Halpin–Tsai and rule of mixture

Using the above formula, weight of the FDM printed parts can be calculated and correspondingly weight fraction can be calculated as follows:

$$\phi = \frac{(w_f / \rho_f)}{\left[ (W_f / \rho_f) + \frac{(1 - W_f - W_v)}{\rho_m} \right]} \tag{9}$$

On using the modified volume fraction in Halpin–Tsai equation, the predicted values showed good agreement with the experimental values (Fig. 20).

Table 5 shows the experimental and predicted values of Young's modulus. It is clear from the tabulated values that the prediction error is reduced in the case of modified Halpin–Tsai model compared to ROM and Halpin–Tsai model.

### 4 Conclusions

A filament modification approach has been proposed for in situ nanocomposite development during FDM 3D printing process. It was found that modifying ABS filament with ABS/OMMT can alter the material properties of the 3D-printed parts. The microstructure and morphology of the nanocomposites showed evidence of nanocomposite formation. The fused network of polymer and OMMT developed during 3D printing contributed to the enhancement of thermal and dielectric properties of the nanocomposite. The presence of stiffer layered silicate improved Young's modulus by 10.8% compared to the pristine polymer. The marginal increase in hardness and decrease in elongation at break were observed for the nanocomposite. The ionic nature of layered silicate provided addition polarization mechanism, thereby increasing the permittivity by 64%. Thermal stability of the nanocomposite was improved due to the restriction offered by OMMT particles on segmental motion of ABS chain. Glass transition temperature was also increased by 6.7°C compared to pristine ABS. The mesostructure of 3D-printed parts was utilized to modify the Halpin–Tsai composite model. It can be concluded that the filament modification of ABS polymer with ABS/OMMT can efficiently enhance the dielectric and thermal properties of the 3D-printed parts.

**Table 5** Comparison between experimental and predictive (rule of mixture, Halpin–Tsai and modified Halpin–Tsai) Young's modulus

Material	Experimental (MPa)	Rule of mixture (MPa)		Halpin–Tsai (MPa)		Modified Halpin–Tsai for FDM (MPa)	
		Predicted	Deviation	Predicted	Deviation	Predicted	Deviation
NC 1	1263.0	1615.2	352.2	1333.0	70.0	1332.0	69.0
NC 3	1314.0	1628.6	314.6	1462.0	148.0	1334.0	20.0
NC 5	1328.0	1631.4	303.0	1478.0	150.0	1334.9	7.0

## References

- Ning F, Cong W, Qiu J, Wei J, Wang S (2015) Additive manufacturing of carbon fiber reinforced thermoplastic composites using fused deposition modeling. *Compos. Part B* 80:369–378
- Chua CK, Leong KF, Lim CS (2003) *Rapid prototyping principles and applications*, 2nd edn. World Scientific, Singapore
- Too MH, Leong KF, Chua CK, Du ZH, Yang SF, Cheah CM, Ho SL (2002) Investigation of 3D non-random porous structures by fused deposition modelling. *Int J Adv Manuf Technol* 19:217–223
- Nikzad M, Masood SH, Sbarski I (2011) Thermo-mechanical properties of a highly filled polymeric composites for fused deposition modeling. *Mater Des* 32:3448–3456
- Moscato S, Bahr R, Le T, Pasian M, Bozzi M, Perregrini L, Tentzeris MM (2016) Infill-dependent 3-D-printed material based on NinjaFlex filament for antenna applications. *IEEE Antennas Wirel Propag Lett* 15:1506–1509
- Masood SH, Song WQ (2004) Development of new metal/polymer materials for rapid tooling using fused deposition modelling. *Mater Des* 25:587–594
- Goh GL et al (2016) Inkjet-printed patch antenna emitter for wireless communication application. *Virtual Phys Prototyp* 11:289–294
- Ahn SH, Montero M, Odell D, Roundy S, Wright PK (2002) Anisotropic material properties of fused deposition modeling ABS. *Rapid Prototyp J* 8:248–257
- Bai J, Goodridge RD, Hague RJM, Song M (2014) Influence of carbon nanotubes on the rheology and dynamic mechanical properties of polyamide-12 for laser sintering. *Polym Test* 36:95–100
- Yuan S, Bai J, Chua CK, Wei J, Zhou K (2016) Highly enhanced thermal conductivity of thermoplastic nanocomposites with a low mass fraction of MWCNTs by a facilitated latex approach. *Compos Part A Appl Sci Manuf* 90:699–710
- Jain PK, Pandey PM, Rao PVM (2009) Selective laser sintering of clay-reinforced polyamide. *Polym Compos* 31:732–743
- Koo JH, Lao S, Ho W, Ngyuen K, Cheng J, Pilato L, Wissler G, Ervin M (2006) Polyamide nanocomposites for selective laser sintering. In: *Proceedings of solid freeform fabrication symposium*, pp 392–409
- Gaikwad S, Tate J, Theodoropoulou N, Koo J (2012) Electrical and mechanical properties of PA11 blended with nanographene platelets using industrial twin-screw extruder for selective laser sintering. *J Compos Mater* 47:2973–2986
- Shofner ML, Lozano K, Rodri FJ (2003) Nanofiber-reinforced polymers prepared by fused deposition modeling. *J Appl Polym Sci* 89:3081–3090
- Francis V, Jain PK (2016) Experimental investigations on fused deposition modelling of polymer-layered silicate nanocomposite. *Virtual Phys Prototyp* 11:109–121
- Francis V, Jain PK (2015) Advances in nanocomposite materials for additive manufacturing. *Int J Rapid Manuf* 5:215–233
- Koo JH (2006) *Polymer nanocomposites processing, characterization, and applications*. McGraw-Hill Nanoscience and Technology Series
- Yan CZ, Shi YS, Yang JS, Liu JH (2011) An organically modified montmorillonite/nylon-12 composite powder for selective laser sintering. *Rapid Prototyp J* 17:28–36
- Sengwa RJ, Choudhary S, Sankhla S (2010) Dielectric properties of montmorillonite clay filled poly(vinyl alcohol)/poly(ethylene oxide) blend nanocomposites. *Compos Sci Technol* 70:1621–1627
- Javadi S, Razzaghi-Kashani M, Gharavi N (2008) The effect of organo-clay on the dielectric properties of silicone rubber. *Smart Mater Struct* 17:365–371
- Azerag B, Azdast T, Doniavi A, Shishavan SM, Lee RE (2015) Structural properties of batch foamed acrylonitrile butadiene styrene/nanoclay nanocomposites. *Int J Mech Mater Eng* 10:19
- Shishavan SM, Azdast T, Ahmadi SR (2014) Investigation of the effect of nanoclay and processing parameters on the tensile strength and hardness of injection molded Acrylonitrile Butadiene Styrene–organoclay nanocomposites. *J Mater* 58:527–534
- Wang S, Hu Y, Zong R, Tang Y, Chen Z, Fan W (2004) Preparation and characterization of flame retardant ABS/montmorillonite nanocomposite. *Appl Clay Sci* 25:49–55
- Singh P, Ghosh AK (2014) Torsional, tensile and structural properties of acrylonitrile–butadiene–styrene clay nanocomposites. *Mater Des* 55:137–145
- Sinha Ray S, Okamoto M (2003) Polymer/layered silicate nanocomposites: a review from preparation to processing. *Prog Polym Sci* 28:1539–1641
- Dimitry OIH, Abdeen ZI, Ismail EA, Saad ALG (2010) Preparation and properties of elastomeric polyurethane/organically modified montmorillonite nanocomposites. *J Polym Res* 17:801–813
- Fulford AR, Wentworth SM (2005) Conductor and dielectric-property extraction using microstrip tee resonators. *Microw Opt Technol Lett* 47:14–16
- Kirschning M, Koster NHL, Jansen RH (1981) Accurate model for open end effect of microstrip lines. *Electron Lett* 17:123–125
- Pluta M, Jeszka JK, Boiteux G (2007) Polylactide/montmorillonite nanocomposites: structure, dielectric, viscoelastic and thermal properties. *Eur Polym J* 43:2819–2835
- Vaia RA, Giannelis EP (1997) Polymer melt intercalation in organically-modified layered silicates: model predictions and experiment. *Macromolecules* 30:8000–8009
- Cao F, Jana SC (2007) Nanoclay-tethered shape memory polyurethane nanocomposites. *Polymer* 48:3790–3800
- Castles F, Isakov D, Lui A, Lei Q, Dancer CEJ, Wang Y, Janurudin JM, Speller SC, Grovenor CRM, Grant PS (2016) Microwave dielectric characterisation of 3D-printed BaTiO<sub>3</sub>/ABS polymer composites. *Sci Rep* 6:22714
- Isakov DV, Lei Q, Castles F, Stevens CJ, Grovenor CRM, Grant PS (2016) 3D printed anisotropic dielectric composite with metamaterial features. *Mater Des* 93:423–430
- Sengwa RJ, Choudhary S, Sankhla S (2009) Dielectric spectroscopy of hydrophilic polymers-montmorillonite clay nanocomposite aqueous colloidal suspension. *Coll Surf A Physicochem Eng Asp* 336:79–87
- Jeszka JK, Pietrzak L, Pluta M, Boiteux G (2010) Dielectric properties of polylactides and their nanocomposites with montmorillonite. *J Non Cryst Solids* 356:818–821
- Francis V, Jain PK (2017) 3D printed polymer dielectric substrates with enhanced permittivity by nanoclay inclusion. *Virtual Phys Prototyp* 12:107–115
- Halpin JLKJC (1976) The Halpin–Tsai equations: a review. *Polym Eng Sci* 16:344–351
- Kalaitzidou K, Fukushima H, Miyagawa H, Drzal LT (2007) Flexural and tensile moduli of polypropylene nanocomposites and comparison of experimental data to Halpin–Tsai and Tandon–Weng models. *Polym Eng Sci* 47:1798–1803
- Sun Q, Rizvi GM, Bellehumeur CT, Gu P (2008) Effect of processing conditions on the bonding quality of FDM polymer filaments. *Rapid Prototyp J* 14:72–80
- Dayma N, Satapathy BK (2010) Morphological interpretations and micromechanical properties of polyamide-6/polypropylene-grafted-maleic anhydride/nanoclay ternary nanocomposites. *Mater Des* 31:4693–4703
- Mohapatra AK, Mohanty S, Nayak SK (2011) Modeling of the mechanical properties of polylactic acid/clay nanocomposites using composite theories. *Int J Plast Technol* 15:174–187